Nanoconfined water in ionic liquid and lyotropic ionic liquid crystals by small- and wide-angle X-ray and neutron scattering: 1-Decyl-3-methylimidazolium nitrate

Hiroshi Abe [a], [*], Fumiya Nemoto [a], Kosuke Hiroi [b], Shinichi Takata [b]

[a] *Department of Materials Science and Engineering, National Defense Academy, Yokosuka 239-8686, Japan*
[b] *J-PARC Center, Japan Atomic Energy Agency, Tokai, Ibaraki 319-1195, Japan*

ABSTRACT

Nanoconfined water (water pocket) and ionic liquid crystals (ILCs) were formed in a hydrophilic ionic liquid (IL)–D_2O system. Herein, 1-decyl-3-methylimidazolium nitrate ($[C_{10}mim][NO_3]$) was used as the IL. By the complementary use of small- and wide-angle X-ray and neutron scattering, a complicated phase diagram of $[C_{10}mim][NO_3]$–D_2O was determined. The lyotropic ILCs of $[C_{10}mim][NO_3]$ containing 70–90 mol% D_2O appeared at room temperature. At high temperature, the lyotropic ILCs transformed into the water pocket in the nanoheterogeneous liquid.

© 20XX

1. Introduction

Ionic liquids (ILs) have been widely used in various fields because of their specific properties [1–11]. Nanoheterogeneous structures are an outstanding feature of ILs that are observed even at room temperature [12–15]. In addition, ILs can be developed into self-organized ionic liquid crystals (ILCs) [16,17]. ILs and ILCs have also been synthesized as functional liquid materials for many industrial applications [18,19].

The nanoheterogeneity of ILs was first predicted by molecular dynamics (MD) [20]. These ILs were from the 1-alkyl-3-methylimidazolium family, $[C_nmim][X]$, where n indicates the alkyl chain length of the cation. Experimentally, the nanoheterogeneity of $[C_nmim][X]$ was investigated using small- and wide-angle X-ray scattering (SWAXS) [21], and MD simulations were performed for pure ILs and hydrophilic IL–water mixtures [22]. In the water-rich region of the $[C_8mim][NO_3]$–water system, the nanoconfined water was shown in the simulation box. Moreover, the nanoconfined water (water pocket) in $[C_nmim][NO_3]$–D_2O (n = 4, 6, and 8) was investigated using small-angle neutron scattering (SANS) [23–25]. A specific water concentration exists in the water pocket, therefore, the crystallization both of $[C_4mim][NO_3]$ and water is suppressed at low temperature [26]. Moreover, the weak hydrogen bonding [27,28] and slow dynamics [29] of $[C_nmim][NO_3]$–water were studied using Raman spectroscopy and quasielastic neutron scattering, respectively. The anomalous static and dynamic properties of the water pocket are summarized in the literature [30].

Phase behaver, surface tension, ionic conductivity, and mesophase structures of aqueous $[C_nmim][X]$ solutions were examined systematically [31], and the phase diagrams of $[C_8mim][X]$–water and $[C_{10}mim][X]$–water (X = Cl or Br) were subsequently determined. Moreover, $[C_8mim][Cl]$ with 69–80 mol% H_2O gelled at room temperature and was classified as a lyotropic ILC [32]. SWAXS results revealed that the lyotropic mesophase contained both hexagonal and lamellar phases. Moreover, the distinct SANS peak of $[C_8mim][Br]$–D_2O and $[C_{10}mim][Br]$–D_2O were obtained [31]. The core–shell ellipsoid model (a Hayter–Penfold model) can fit the observed SANS peak. Small-angle X-ray scattering revealed that a two-dimensional (2D) hexagonal structure was formed in $[C_{10}mim][NO_3]$–78.8 mol% H_2O [33]. Furthermore, a distinct peak appeared in the SANS pattern in $[C_{12}mim][NO_3]$–D_2O [34].

Water-in-salt, which is another type of nanoconfined water, exhibited high performance in lithium-ion batteries [35]. The water-in-salt electrolytes contain $Li(H_2O)_{2.5}$–TFSI (TFSI = bis(trifluoromethanesulfonyl)imide). Moreover, IL-assisted water-in-salt electrolytes can improve the electrochemical stability of devices [36]. In contrast, in the self-assembled ILCs, 1D, 2D or 3D nanochannel networks were designed freely, and water transportation was tuned for their tasks [37]. The hydrogen bonding states of nanoconfined waters were simulated using

* Corresponding author.
  E-mail address: ab@nda.ac.jp (H. Abe).

MD. The properties of nanoconfined water in mixed systems were summarized in previous studies [38,39].

In this study, we determined the complicated phase diagram of $[C_{10}mim][NO_3]$–D_2O using SWAXS and small- and wide-angle neutron scattering (SWANS). The lyotropic mesophase was investigated only by SWANS. A complementary use of X-ray and neutron scattering was used to determine the 2D hexagonal structure of the lyotropic ILCs.

2. Experimental method

2.1. Materials

The hydrophilic IL used in this study was $[C_{10}mim][NO_3]$, which was purchased from Angene Chemical, Co. (>98.0%). The as-received sample was vacuum dried at room temperature using a diaphragm vacuum pump (DTU-20, Ulvac Co.). The phase behavior of pure $[C_nmim][NO_3]$ (n = 2, 4, 6, 8, and 10) is summarized in Table 1 [40]. The solidification of pure $[C_nmim][NO_3]$ (n = 2, 4, 6, 8, and 10) did not occur at room temperature.

Considering the neutron scattering length density (SLD), distilled D_2O (99.9%, Merck Co.) was selected as an additive to enhance the water pocket. The mixture of hydrophilic IL and D_2O was prepared inside a glove box under flowing helium gas to avoid contact with atmospheric moisture. The $[C_{10}mim][NO_3]$–x mol% D_2O systems with 70, 80, and 90 mol% D_2O existed as solids at 23 °C (Fig. S1).

2.2. Simultaneous measurements of small- and wide-angle X-ray scattering and differential scanning calorimetry

To clarify the complicated phase behavior of $[C_{10}mim][NO_3]$–D_2O at low temperature, a differential scanning calorimetry (DSC) instrument was attached to the X-ray diffractometer (SmartLab, Rigaku Co.) [41]. Simultaneous SWAXS and DSC measurements were conducted using Cu Kα radiation (λ = 1.542 Å). Here the scattering vector Q was defined as $4\pi(\sin\theta)/\lambda$ (Å^{-1}), where 2θ is the scattered angle. Metal-coated Mylar films were used as DSC windows in SWAXS. The temperature range for the simultaneous measurements was from –95 °C to 80 °C. The cooling/heating rate was 5 °C/min. During the simultaneous measurements, dry nitrogen gas was flown at 20 mL/min to reduce moisture.

SLDs for the X-ray scattering were calculated using the observed densities in Table 2 [42,43]. During X-ray diffraction, D_2O in the ILs is often difficult to investigate. For instance, the normalized SLD of $[C_8mim][Cl]$–D_2O during X-ray diffraction is plotted in Fig. S2. Since the normalized SLD only slightly depends on D_2O concentration, the SLD of $[C_8mim]^+$ mainly contributes to the total X-ray scattering intensity.

Table 1
Phase behavior of pure $[C_nmim][NO_3]$ (n = 2, 4, 6, 8, and 10) [40].

$[C_nmim][NO_3]$	n = 2	n = 4	n = 6	n = 8	n = 10
	Cryst.	Glass.	Glass	Glass	Cryst.
	T_C = -10.7 °C	T_g ~ -41 °C	T_g ~ -70 °C	T_g ~ -71 °C	T_C = -17.3 °C

Table 2
X-ray and neutron scattering length densities (SLDs) of $[C_8mim][Cl]$ and $[C_8mim][NO_3]$ obtained using the observed densities [42,43].

				SLD ($\times 10^{-6}$ Å^{-2})	
		$\rho(g/cm^3)$	25 °C	X-ray	neutron
$[C_8mim][Cl]$	pure	[42]	1.008810	9.396	0.5802
$[C_8mim][Cl]$	78.33 mol% H_2O	[42]	1.010423	9.189	1.928
$[C_8mim][NO_3]$	pure	[43]	1.074	9.950	0.9861

2.3. Small- and wide-angle neutron scattering

SWANS experiments were conducted on a BL15 instrument (TAIKAN) at the Japan Proton Accelerator Research Complex (J-PARC) [44]. To observe the hierarchical structure in the wide Q-range, small-, medium-, and high-angle detector banks were equipped on the TAIKAN instrument. A sample changer was mounted onto the goniometer, and the temperature was controlled with a circulating bath (Ministat 125, Huber, Co.). The mixtures were inserted into a 1.0-mm thick quartz cell (Starna Scientific Ltd.) with a low neutron absorption ability. We analyzed the observed data quantitatively using background intensities such as those of the empty cell, glassy carbon, and D_2O-filled-cell.

SLDs for neutrons were also estimated (Table 2). In a previous study [25], small neutron SLD values of $[C_nmim]^+$ were calculated. The normalized SLD for neutrons in Fig. S2 indicates that D_2O is more observable in the water-rich region of $[C_8mim][Cl]$–D_2O. Therefore, the water pocket is enhanced in SWANS.

3. Results and discussion

3.1. Small- and wide-angle X-ray scattering and differential scanning calorimetry of $[C_{10}mim][NO_3]$ – D_2O

$[C_{10}mim][NO_3]$ with 70–90 mol% D_2O existed in the solid state at room temperature (Fig. S1). In a previous study [33], $[C_{10}mim][NO_3]$–78.8 mol% H_2O formed a strong physical gel at room temperature. For instance, the gelation of $[C_{10}mim][NO_3]$–80 mol% D_2O was observed at approximately 60 °C (T_{hex}).

The water concentration dependence of the phase behavior of $[C_{10}mim][NO_3]$–x mol % D_2O was obtained by the simultaneous SWAXS and DSC measurements. Fig. 1 shows the SWAXS patterns of $[C_{10}mim][NO_3]$–x mol % D_2O as a function of water concentration at the minimum temperature (T_{min} = –95 °C). For comparison, the SWAXS pattern of pure $[C_{10}mim][NO_3]$ at T_{min} is plotted in Fig. 1. In the pure system, the 00ℓ Bragg reflections (ℓ = 1, 2, 3, and 5) indicated a hybrid layered structure with a large lattice constant of 42.1 Å [42]. The Q_{001} of the hybrid layered structure was 0.15 Å^{-1} (Q_{hyb}). At 60–95 mol% D_2O, the 00ℓ Bragg reflections were also observed at T_{min}. Compared with the SWAXS pattern of the pure system, some additional Bragg reflections were observed for the 60–95 mol% mixtures. This indicates that the hybrid layered structure could be modified slightly by the addition of water. The 97.5 mol% mixture exhibited a different SWAXS pattern at T_{min} (Fig. 1). Moreover, the Q_{001} Bragg reflection of the hybrid layered structure vanished in the SWAXS pattern of $[C_{10}mim][NO_3]$–97.5 mol% D_2O. The stacking sequence of the 97.5 mol% mixture was represented by the lattice constant of 25.2 Å. In a previous study [42], the ILC-like crystal of pure $[C_{10}mim][NO_3]$ was induced by a specific cooling rate, and the ILC-like crystal was identified by the sharp Bragg reflection at Q_{pre}. Moreover, the ice crystal coexisted in the 97.5 mol% mixture due to its weak Bragg reflections.

Enthalpy was calculated from the DSC traces. For instance, the enthalpy change in ethylammonium nitrate (EAN)–water as an ideal system was estimated [45]. Fig. 2 indicates the water concentration dependence of the enthalpy difference, ΔH, upon cooling of $[C_{10}mim][NO_3]$–D_2O. Here, the ΔH of cold crystallization upon heating does not contribute to the ΔH in Fig. 2. The broken line in Fig. 2 indicates the ideal enthalpy difference for IL crystallization [45]. Within the experimental errors, the smaller ΔH values of 70–90 mol% D_2O were caused by partial amorphization upon cooling or cold crystallization upon heating. In contrast to EAN–H_2O, the crystallization of $[C_{10}mim][NO_3]$–D_2O occurred over the whole water concentration region.

The simultaneous SWAXS-DSC measurements of $[C_{10}mim][NO_3]$–80 mol% D_2O were conducted between –95 and 80 °C (Fig. 3). At 80 °C before cooling, a broad prepeak at 0.25 Å^{-1} (Q_{pre}) appeared in the
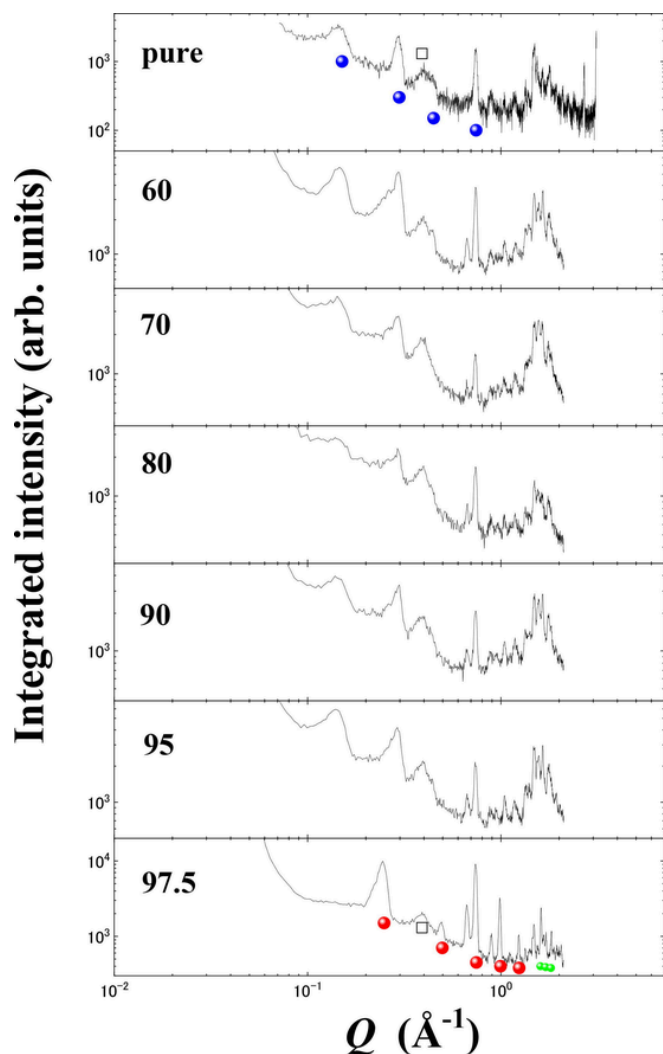
Fig. 1. Water concentration dependence of small- and wide-angle X-ray scattering (SWAXS) patterns at − 95 ℃. The open square reveals the scattering from the DSC windows. Blue closed circles represent the hybrid layered structure. Red and green closed circles reveal the ionic liquid crystal-like and ice crystal structures, respectively.

Fig. 2. Enthalpy difference, ΔH, between the liquid and solid states as a function of water concentration x. The dotted line indicates the ideal ΔH of $[C_{10}mim][NO_3]$.

$[C_{10}mim][NO_3]$ and X-ray insensitive D_2O crystallized at T_{CC} upon heating. At 23.6 ℃ (T_m), the $[C_{10}mim][NO_3]$ crystals melted with a distinct endothermal peak. After further heating, no change was observed in both the SWAXS pattern and DSC thermal trace. Hence, even upon heating, the gel-melting at T_{hex} (~60 ℃) was not investigated using X-ray scattering.

The phase behavior of $[C_{10}mim][NO_3]$–97.5 mol% D_2O was obtained by the simultaneous SWAXS and DSC measurements (Fig. 4). The prepeak of the liquid mixture at 30 ℃ was located at 0.20 Å⁻¹. The relatively long correlation length of 31.4 Å was caused by the presence of an excess amount of water. Upon cooling, a sharp exothermal peak was observed at –19.3 ℃ (T_{C1}) (Fig. 4). Subsequently, another sharp exothermal peak appeared at –30.1 ℃ (T_{C2}). Due to the weak incident X-ray intensity of SWAXS and the slow scanning, the phases at T_{C1} and T_{C2} were not distinguished. However, ice crystals could be formed at T_{C1} considering the coexistence of ice and the ILC-like crystals at T_{min} (Fig. 1). We confirm that the ILC-like crystals appeared at T_{C2}. Just below T_{C2}, the peak position of the 001 Bragg reflection (0.21 Å⁻¹) in the ILC-like crystals was higher than that in the liquid state. Upon heating, cold crystallization was observed at –31.7 ℃, and the SWAXS pattern varied at T_{CC}. Both ILC-like and ice crystals melted subsequently at approximately –13.2 ℃ (T_m).

3.2. Small- and wide-angle neutron scattering of $[C_{10}mim][NO_3] – D_2O$

Information on D_2O in the mixtures was obtained using the large SLD of D_2O for neutron scattering (Fig. S2). The SWANS patterns of $[C_{10}mim][NO_3] – D_2O$ at 30 ℃ are shown in Fig. 5. At 30 ℃, pure $[C_{10}mim][NO_3]$ in the liquid state exhibited a prepeak at Q_{pre}. Since $[C_{10}mim]^+$ possesses a small SLD for neutron scattering, the prepeak in the pure system is mainly derived from $[NO_3]^-$, whose SLD for neutron scattering is intermediate [25]. In $[C_{10}mim][NO_3] – 60$ mol% D_2O, the mixture was in liquid state at 30 ℃ (Fig. S1). As the peak intensity increased, the peak shifted to a lower Q position. Considering the large neutron SLD of D_2O, it was found that a water pocket is formed in $[C_{10}mim][NO_3] – 60$ mol% D_2O. Using neutron scattering, a significant finding was obtained for gel $[C_{10}mim][NO_3] – 70$ mol% D_2O at 30 ℃ (Fig. 5). A sharp and intense peak appeared at 0.22 Å⁻¹. In addition, two weak Bragg reflections were observed at 0.38 and 0.44 Å⁻¹. For the 2D hexagonal structures, Bragg reflections are expressed by Q_{hk} [46]. The 0.22, 0.38, and 0.44 Å⁻¹ Bragg reflections at 70 mol% D_2O were indexed as 10, 11, and 20, respectively, on the 2D reciprocal lattice plane.

SWAXS pattern of the liquid mixture. In the pure $[C_{10}mim][NO_3]$ system at room temperature [42], a prepeak was observed at 0.23 Å⁻¹. The prepeak of the pure system is derived from the nanoheterogeneity of the liquid structure. The correlation length of the nanoheterogeneity at 80 ℃ was evaluated to be 25.1 Å. The nanoheterogeneity of the pure system existed even at 80 mol% D_2O above T_{hex}. Since $[C_{10}mim]^+$ is quite sensitive to X-rays, the prepeak of the mixture was derived mainly from $[C_{10}mim]^+$. Upon cooling, the SWAXS patterns and DSC thermal trace at T_{hex} did not change at all (Fig. 3). We could not observe the phase change at T_{hex} using the simultaneous SWAXS and DSC measurements. This result is in contrast to the solidification observed at T_{hex}. Thus, we deduce that X-ray insensitive D_2O is only related to the gelation at T_{hex}. After further cooling, a distinct phase transition occurred at T_{C1} (=–15.5 ℃), and an exothermal peak was observed on the DSC thermal trace (Fig. 3). In addition, the Bragg reflections were observed in the SWAXS pattern after the disappearance of the prepeak. Due to the small SLD of D_2O in the SWAXS profiles, it is difficult to recognize the ice crystal formation in $[C_{10}mim][NO_3]$–80 mol% D_2O. Upon heating, cold crystallization occurred at –33.0 ℃ (T_{CC}) with an exothermal peak (Fig. 3). However, no change was observed at T_{CC} in the SWAXS patterns. Therefore, we assumed that the partially amorphized
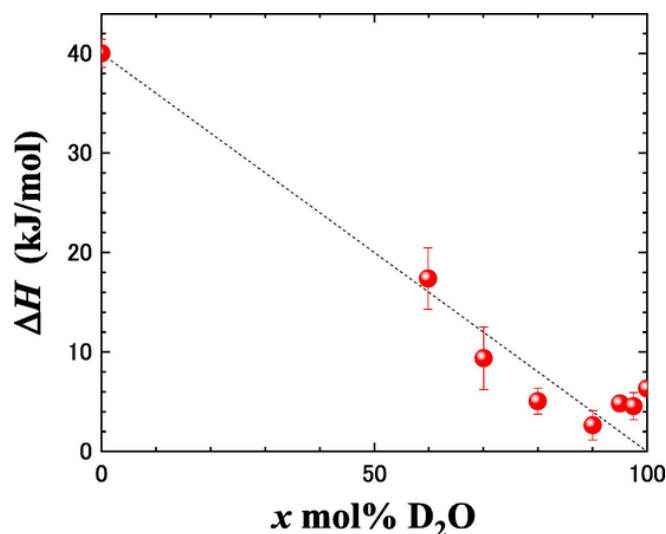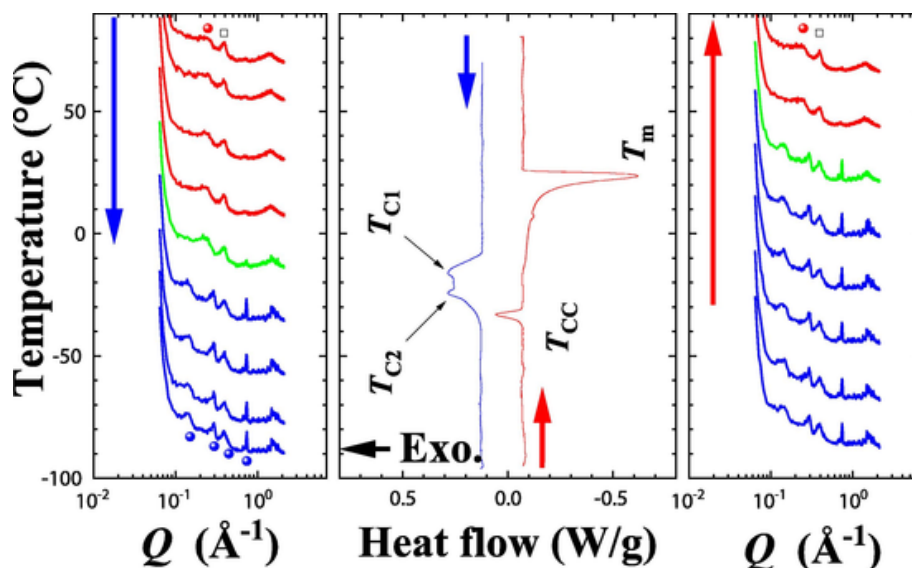
Fig. 3. Small- and wide-angle X-ray scattering (SWAXS) and differential scanning calorimetry (DSC) thermal trace of $[C_{10}mim][NO_3]$ − 80 mol% D_2O. Open square reveals the scattering from the DSC windows. In the SWAXS pattern, the prepeak position (Q_{pre}) in the liquid state is expressed by red closed circles. Closed blue circles indicate the 00ℓ Bragg reflections (ℓ = 1, 2, 3, and 5) of the hybrid layered structure. T_{C1} and T_{C2} are phase transition temperatures, and T_{CC} corresponds to the cold crystallization temperature upon heating. T_m is the melting point of the hybrid layered structure.
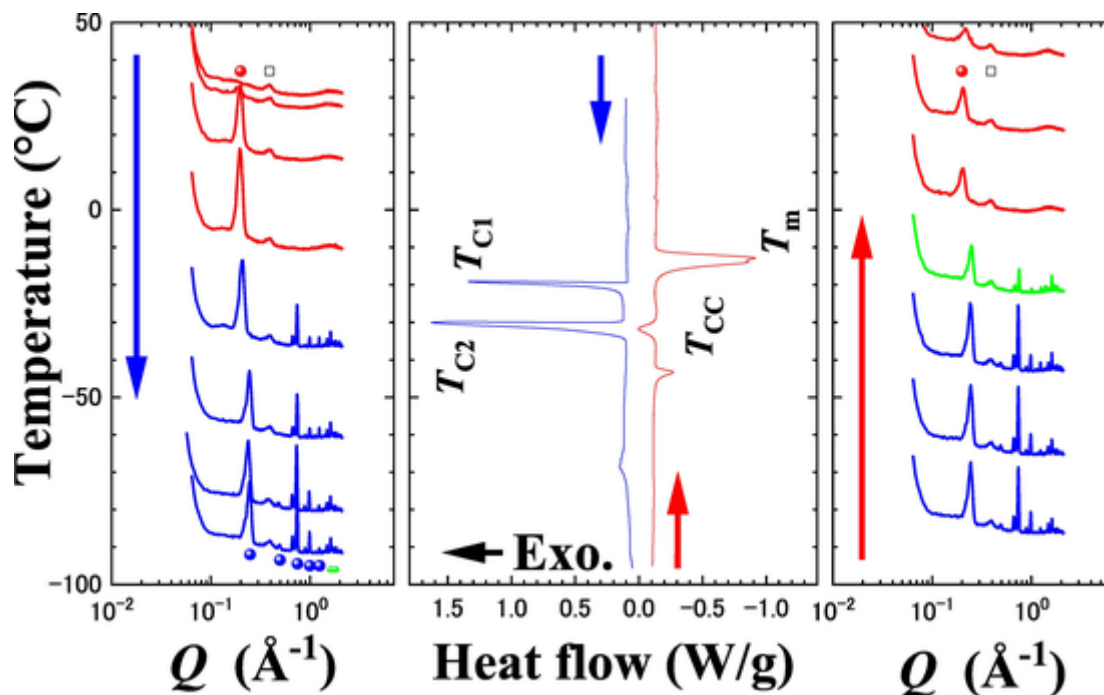

Fig. 4. Small- and wide-angle X-ray scattering (SWAXS) and differential scanning calorimetry (DSC) thermal trace of $[C_{10}mim][NO_3]$ − 97.5 mol% D_2O. Open square reveals the scattering from the DSC windows. In the SWAXS pattern, the prepeak position (Q_{pre}) in the liquid state is expressed by closed red circles. Closed blue circles indicate the 00ℓ Bragg reflections (ℓ = 1, 2, 3, 4, and 5) of the ionic liquid crystal (ILC)-like crystals. T_{C1} and T_{C2} are phase transition temperatures, while T_{CC} corresponds to the cold crystallization temperature upon heating. T_m is the melting point of the ILC-like crystal.

On the Q plot (Fig. 5), $Q_{11} = \sqrt{3}Q_{10}$ was satisfied for gel $[C_{10}mim][NO_3]$ − 70 mol% D_2O. The hexagonal lattice constant, a_{hex}, at 70 mol% was 32.76 Å. Certainly, gelation as the lyotropic mesophase occurred in $[C_{10}mim][NO_3]$ − 78.8 mol% H_2O and was analyzed using synchrotron X-ray scattering [32]. Hence, it was found that the solidification at T_{hex} is caused by the gelation. Although the gelation was not detected using conventional SWAXS and weak incident X-rays (Fig. 1), the D_2O-mediated 2D hexagonal structure was extracted by neutron scattering. Using the complimentary use of SWAXS and SWANS, we em-

phasize that the lyotropic mesophase contained the frozen nanoheterogeneous $[C_{10}mim]^+$ and 2D hexagonal structure of D_2O. The peak of gel $[C_{10}mim][NO_3]$ − 80 mol% D_2O coincided with that of $[C_{10}mim][NO_3]$ − 70 mol% D_2O. The a_{hex} of the 80 mol% mixture was calculated to be 33.26 Å. At 90 mol% D_2O, an obvious peak shift and an increase in the peak intensity were observed. A peak shift to the lower Q position implies that the 2D hexagonal structure developed due to a large amount of water. Moreover, the a_{hex} of the 90 mol% mixture was found to be 36.85 Å. Above 95 mol%, the 2D hexagonal structure col-
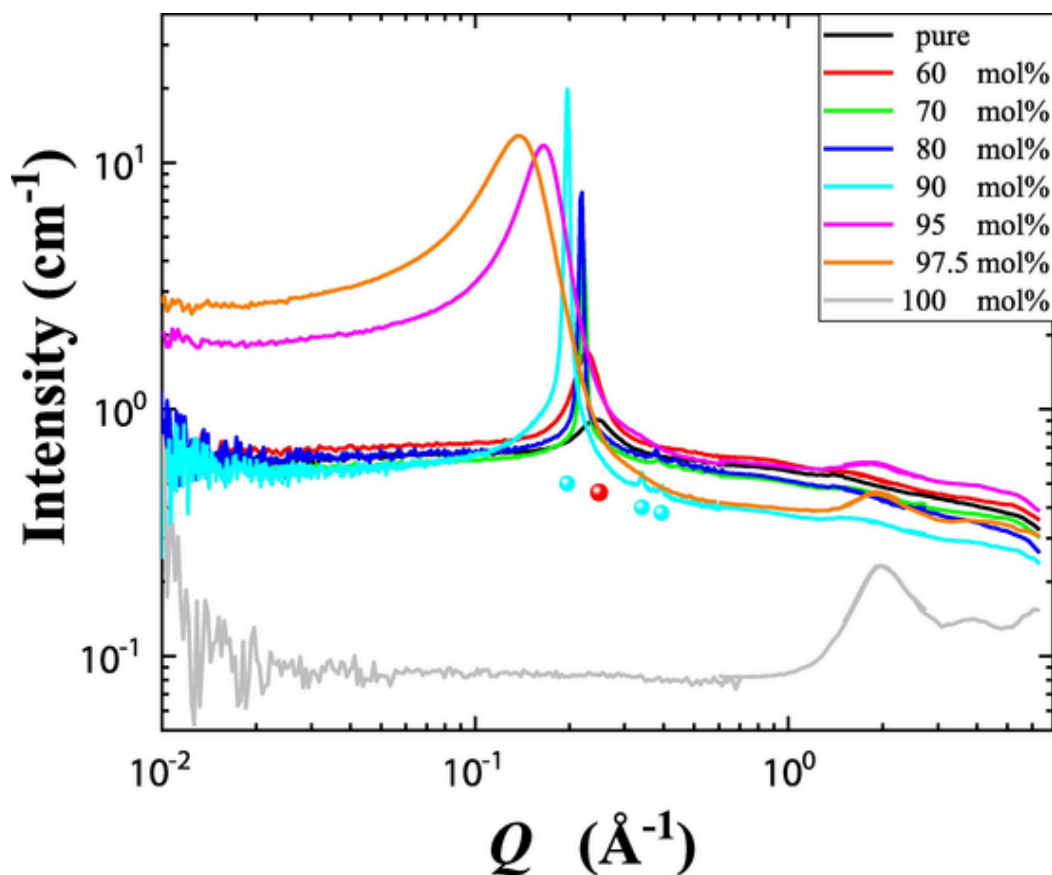
Fig. 5. Water concentration dependence of small- and wide-angle neutron scattering (SWANS) at 30 ℃. The closed red circle indicates the prepeak position. Closed light-blue circles correspond to the 10, 11, and 20 Bragg reflections of the 2D hexagonal reciprocal lattice.

lapsed at 30 ℃, and water was percolated over the whole region (Fig. 5).

Based on its SWANS pattern, the $[C_{10}mim][NO_3]$ − 80 mol% D_2O gel is regarded as the lyotropic ILC at 30 ℃. To compare T_{hex} determined by visual observation, the SWANS patterns of $[C_{10}mim][NO_3]$ − 80 mol% D_2O were collected at an elevated temperature (Fig. 6). Obviously, the Bragg reflections of the 2D hexagonal lattice disappeared at 60 ℃. Instead, a broad peak appeared near the Q_{pre} position, which corresponded to the water pocket in $[C_{10}mim][NO_3]$ − 80 mol% D_2O. The correlation length between the water pockets was 28.56 Å at 60 ℃. With increasing temperature and decreasing the intensity, the broad peak shifted to a higher Q position. Notably, the water pocket existed even at 80 ℃. To determine the water pocket region on the phase diagram precisely, we measured the temperature dependence of the SANS patterns in pure IL and other mixtures (Fig. 7). By visual observation, the T_{hex} of $[C_{10}mim][NO_3]$ − 70 mol% was found to be 33 ℃. Thus, the SANS data were consistent with the visual observation. With increasing temperature, the broad peak representing the water pocket existed up to 80 ℃. In the MD simulations of $[C_8mim][NO_3]$ − H_2O [22], water was percolated over the whole region at 95.2 mol% H_2O. Similarly, the SANS profiles of $[C_{10}mim][NO_3]$ − 95 mol% D_2O and $[C_{10}mim][NO_3]$ − 97.5 mol% D_2O showed the presence of percolated D_2O. More importantly, the water percolated at the water-rich region did not transform into the water pocket at 80 ℃. The percolated water was stable even at 80 ℃. Hence, above 95 mol%, the water pocket cannot exist at any temperature.

3.3. Phase diagram and structure models of $[C_{10}mim][NO_3]$ − D_2O

The low-temperature complicated phase behavior of $[C_{10}mim][NO_3]$ − x mol% D_2O is depicted in the phase diagram given

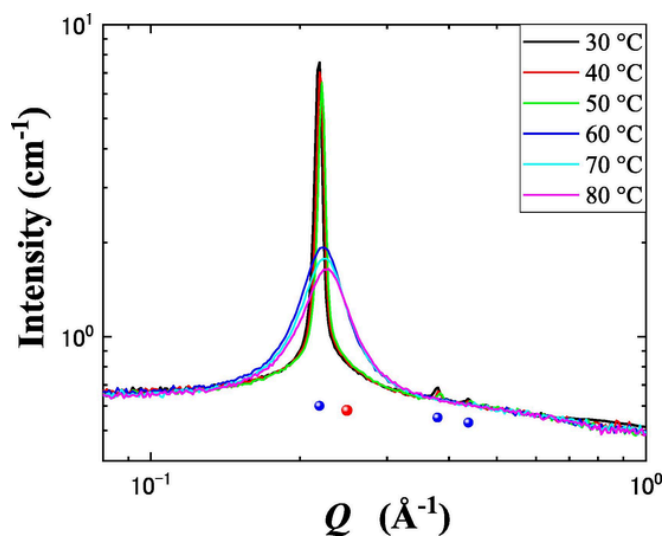**Fig. 6.** Temperature dependence of small- and wide-angle neutron scattering (SWANS) patterns in $[C_{10}mim][NO_3]$ − 80 mol% D_2O. The closed red circle indicates the prepeak position. Closed blue circles correspond to the 10, 11, and 20 Bragg reflections of the 2D hexagonal reciprocal lattice.

in Fig. 8. Water concentration and temperature dependences of the SWANS patterns can clarify the phase changes of $[C_{10}mim][NO_3]$ − D_2O. Particularly, a relationship between the water pocket and lyotropic mesophase is first obtained on the phase diagram. Simultaneously, the percolated water in the water-rich region is related to the ILC-like crystal.
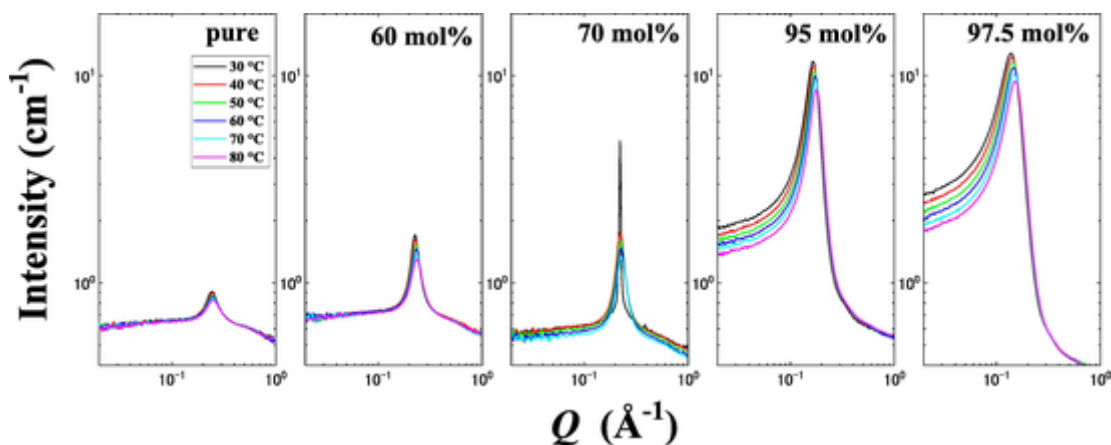
Fig. 7. Temperature dependence of the small-angle neutron scattering (SANS) patterns of $[C_{10}mim][NO_3] - x$ mol% D_2O.

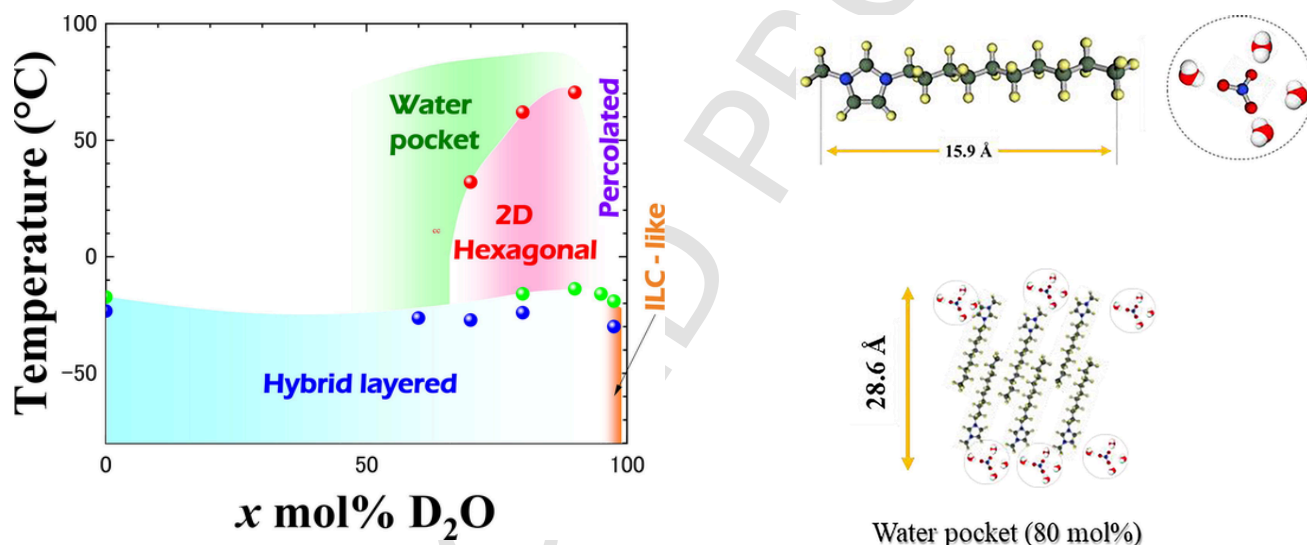**Fig. 8.** Phase diagram of $[C_{10}mim][NO_3] - D_2O$ determined by small- and wide-angle X-ray and neutron scattering (SWANS).

Water pocket (80 mol%)

Fig. 9. Structure model of the water pocket in the partial 2D layers and the lyotropic mesophase in the 2D hexagonal lattice.

The ILC phase of pure $[C_{10}mim][NO_3]$ was simulated using MD [47]. The 2D layered structure of the ILC phase is related to the prepeak of the pure system. Moreover, in the previous study [48], the hydrating water molecules in nitrate aqueous solutions were estimated using Raman spectroscopy. By changing the water concentrations, the 718 cm^{-1} Raman band was found to be in-plane deformation of the hydrated nitrate ions. In case of $[C_8mim][NO_3]$-D_2O [28], the 718 cm^{-1} band existed in the water-rich region. In $[C_{10}mim][NO_3] - 80$ mol% D_2O, the molecular ratio is as follows: $[C_{10}mim][NO_3]$:$D_2O = 1$:4. Based on the hydrated nitrate, the water pocket of $NO_3(D_2O)_4$ is introduced (Fig. 9). Considering the cation size and correlation length (28.6 Å) between the water pockets, a partial 2D liquid structure of $[C_{10}mim][NO_3] - 80$ mol% D_2O was considered, wherein the alkyl chains of the $[C_{10}mim]^+$ cation were stacked each other while satisfying the correlation length (Fig. 9). Because the water pocket existed in the liquid state without a periodicity, the water pocket was distributed randomly on the partial 2D layers. Furthermore, we introduce the structure model of the 2D hexagonal lattice ($a_{hex} = 33.3$ Å) to explain the observed SWAXS and SWANS patterns: (i) the $[C_{10}mim]^+$ cation is frozen in nanoheterogeneity, and (ii) the water pocket including the $[NO_3]^-$ anion is in an ordered state. The $[C_{10}mim]^+$ cations are not illustrated in Fig. 9. If we assume that the density of $[C_{10}mim][NO_3]$ –80 mol% D_2O is ~ 1 g/cm³, 6 cations, 6 anions, and 24 water molecules could be included in the hexagonal unit cell (two triangles). The

phase transition from the water pocket to the 2D hexagonal lattice at T_{hex} without an exothermal peak implies that the water aggregates could not be collapsed. In addition, the sharp Bragg reflections of the lyotropic mesophase indicate that the neutron-sensitive D_2O is well or-

dered. Thus, we assume that the water aggregation of $(NO_3)_3(D_2O)_{12}$ in one triangle is formed on the 2D hexagonal lattice (Fig. 9). In the 90 mol% mixtures, the molecular ratio becomes $[C_{10}mim][NO_3]:D_2O = 1:9$. Considering the density of ~ 1 g/cm^3, the $(NO_3)_3(D_2O)_{27}$ aggregation could occur in one triangle. The $(NO_3)_3(D_2O)_{27}$ aggregation also explains the a_{hex} of 36.9 Å in $[C_{10}mim][NO_3]$ − 90 mol% D$_2$O. When the phase transition from the 2D hexagonal lattice to the hybrid layered structure occurred at T_{C1}, frozen nanoheterogeneous $[C_{10}mim]^+$ transformed to a well-orientated ordered array with a distinct exothermal peak (Fig. 3). Furthermore, the molecular rearrangement at T_{C1} indicates that the well-ordered water aggregates vanish.

4. Conclusions

Various phases of $[C_{10}mim][NO_3]$ − D$_2$O were investigated by the complementary use of SWAXS and SWANS. $[C_{10}mim][NO_3]$ − D$_2$O exhibits a complicated phase diagram, in which nanoconfined water (water pocket) appears near the lyotropic ILC region having a 2D hexagonal lattice. The phase transition from the water pocket to the lyotropic ILC is explained by aggregation rearrangement from the partial 2D array of the water pocket to the large water aggregation in the well-ordered 2D hexagonal lattice. Above 95 mol% D$_2$O, the lyotropic ILC collapsed because of the presence of an excess amount of water. In the specific water concentration region of $70 \leq x \leq 90$ mol%, a 2D periodic array of large water aggregates was formed spontaneously in the lyotropic ILC. The size-tunable water aggregation in the periodic lattice can be utilized in next-generation nanoheterogeneity engineering.

CRediT authorship contribution statement

Hiroshi Abe : Conceptualization, Writing – original draft, Writing – review & editing. **Fumiya Nemoto :** Formal analysis. **Kosuke Hiroi :** Data curation, Formal analysis. **Shinichi Takata :** Data curation, Formal analysis.

Declaration of Competing Interest

The authors declare that they have no known competing financial interests or personal relationships that could have appeared to influence the work reported in this paper.

Data availability

Data will be made available on request.

Acknowledgments

Appendix A. Supplementary data

Supplementary data to this article can be found online at https://doi.org/10.1016/j.molliq.2023.122551.

References

[1] Z. Lei, B. Chen, Y.-M. Koo, D.R. MacFarlane, Introduction: Ionic Liquids, Chem. Rev. 117 (2017) 6633–6635.
[2] T. Welton, Room-Temperature Ionic Liquids. Solvents for Synthesis and Catalysis, Chem. Rev. 99 (1999) 2071–2083.
[3] Y. Qiao, W. Ma, N. Theyssen, C. Chen, Z. Hou, Temperature-Responsive Ionic Liquids: Fundamental Behaviors and Catalytic Applications, Chem. Rev. 117 (2017) 6881–6928.
[4] M. Armand, F. Endres, D.R. MacFarlane, H. Ohno, B. Scrosati, Ionic-liquid materials for the electrochemical challenges of the future, Nature Mater. 8 (2009) 621–629.
[5] M. Watanabe, M.L. Thomas, S. Zhang, K. Ueno, T. Yasuda, K. Dokko, Application of Ionic Liquids to Energy Storage and Conversion Materials and Devices, Chem. Rev. 117 (2017) 7190–7239.
[6] L.A. Blanchard, D. Hancu, E.J. Beckman, J.F. Brennecke, Green processing using ionic liquids and CO$_2$, Nature 399 (1999) 28–29.
[7] Z. Lei, C. Dai, B. Chen, Gas Solubility in Ionic Liquids, Chem. Rev. 114 (2014) 1289–1326.
[8] S. Zeng, X. Zhang, L. Bai, X. Zhang, H. Wang, J. Wang, D. Bao, M. Li, X. Liu, S. Zhang, Ionic-Liquid-Based CO$_2$ Capture Systems: Structure, Interaction and Process, Chem. Rev. 117 (2017) 9625–9673.
[9] A. Pinkert, K.N. Marsh, S. Pang, M.P. Staiger, Ionic Liquids and Their Interaction with Cellulose, Chem. Rev. 109 (2009) 6712–6728.
[10] H. Wang, G. Gurau, R.D. Rogers, Ionic liquid processing of cellulose, Chem. Soc. Rev. 41 (2012) 1519–1537.
[11] S.P.M. Ventura, F.A. e Silva, M.V. Quental, D. Mondal, M.G. Freire, J.A.P. Coutinho, Ionic-Liquid-Mediated Extraction and Separation Processes for Bioactive Compounds: Past, Present, and Future Trends, Chem. Rev. 117 (2017) 6984–7052.
[12] R. Hayes, G.G. Warr, R. Atkin, Structure and Nanostructure in Ionic Liquids, Chem. Rev. 115 (2015) 6357–6426.
[13] K. Dong, X. Liu, H. Dong, X. Zhang, S. Zhang, Multiscale Studies on Ionic Liquids, Chem. Rev. 117 (2017) 6636–6695.
[14] S. Zhang, J. Zhang, Y. Zhang, Y. Deng, Nanoconfined Ionic Liquids, Chem. Rev. 117 (2017) 6755–6833.
[15] Y.-L. Wang, B. Li, S. Sarman, F. Mocci, Z.-Y. Lu, J. Yuan, A. Laaksonen, M.D. Fayer, Microstructural and Dynamical Heterogeneities in Ionic Liquids, Chem. Rev. 120 (2020) 5798–5877.
[16] K. Binnemans, Ionic Liquid Crystals, Chem. Rev. 105 (2005) 4148–4204.
[17] K. Goossens, K. Lava, C.W. Bielawski, K. Binnemans, Ionic Liquid Crystals: Versatile Materials, Chem. Rev. 116 (2016) 4643–4807.
[18] A.A.C. Toledo Hijo, G.J. Maximo, M.C. Costa, E.A.C. Batista, A.J.A. Meirelles, Applications of Ionic Liquids in the Food and Bioproducts Industries, ACS Sustainable, Chem. Eng. 4 (2016) 5347–5369.
[19] K. Salikolimi, A.A. Sudhakar, Y. Ishida, Functional Ionic Liquid Crystals, Langmuir 36 (2020) 11702–11731.
[20] J.N.A. Canongia Lopes, A.A.H. Pádua, Nanostructural Organization in Ionic Liquids, J. Phys. Chem. B 110 (2006) 3330–3335.
[21] A. Triolo, O. Russina, H.-J. Bleif, E.D. Cola, Nanoscale Segregation in room temperature ionic liquids, J. Phys. Chem. B 111 (2007) 4641–4644.
[22] W. Jiang, Y. Wang, G.A. Voth, Molecular dynamics simulation of nanostructural organization in ionic liquid/water mixtures, J. Phys. Chem. B 111 (2007) 4812–4818.
[23] H. Abe, T. Takekiyo, M. Shigemi, Y. Yoshimura, S. Tsuge, T. Hanasaki, K. Ohishi, S. Takata, J. Suzuki, Direct Evidence of Confined Water in Room-Temperature Ionic Liquids by Complementary Use of Small-Angle X-ray and Neutron Scattering, J. Phys. Chem. Lett. 5 (2014) 1175–1180.
[24] H. Abe, T. Takekiyo, M. Shigemi, Y. Yoshimura, S. Tsuge, T. Hanasaki, K. Ohishi, S. Takata, J. Suzuki, Size-tunable Confined Water in a Room Temperature Ionic Liquid, JPS Conf. Proc. 8 (2015) 033001–033006.
[25] H. Abe, F. Nemoto, K. Hiroi, K. Ohishi, S. Takata, Spontaneous formations of nanoconfined water in ionic liquids by small-angle neutron scattering, J. Mol. Liq. 346 (2022) 117035–117036.
[26] H. Abe, T. Takekiyo, Y. Yoshimura, K. Saihara, A. Shimizu, Anomalous Freezing of Nano-Confined Water in Room-Temperature Ionic Liquid 1-Butyl-3-Methylimidazolium Nitrate, ChemPhysChem 17 (2016) 1136–1142.
[27] H. Abe, T. Takekiyo, M. Aono, H. Kishimura, Y. Yoshimura, N. Hamaya, Polymorphs in room-temperature ionic liquids: Hierarchical structure, confined water and pressure-induced frustration, J. Mol. Liq. 210 (2015) 200–214.
[28] H. Abe, Y. Yoshiichi, T. Hirano, T. Ohkubo, H. Kishimura, Hydrogen bonding of nanoconfined water in ionic liquids, J. Mol. Liq. 367 (2022) 120383–120388.
[29] H. Abe, T. Yamada, K. Shibata, Dynamic properties of nano-confined water in an ionic liquid, J. Mol. Liq. 264 (2018) 54–57.
[30] H. Abe, T. Takekiyo, Y. Yoshimura, A. Shimizu, Static and dynamic properties of nano-confined water in room-temperature ionic liquids, J. Mol. Liq. 290 (2019) 111216–111219.
[31] I. Goodchild, L. Collier, S.L. Millar, I. Prokeš, J.C.D. Lord, C.P. Butts, J. Bowers, J.R.P. Webster, R.K. Heenan, Structural studies of the phase, aggregation and surface behaviour of 1-alkyl-3-methylimidazolium halide + water mixtures, J. Colloid Interface Sci. 307 (2007) 455–468.
[32] A.L. Sturlaugson, A.Y. Arima, H.E. Bailey, M.D. Fayer, Orientational Dynamics in a Lyotropic Room Temperature Ionic Liquid, J. Phys. Chem. B 117 (2013) 14775–14784.
[33] B.T. Nebgen, H.D. Magurudeniya, K.W.C. Kwock, B.S. Ringstrand, T. Ahmed, S. Seifert, J.-X. Zhu, S. Tretiak, M.A. Firestone, Design principles from multiscale simulations to predict nanostructure in self-assembling ionic liquids, Faraday Discuss. 206 (2018) 159–181.
[34] T. Takamuku, T. Shimomura, K. Sadakane, M. Koga, H. Seto, Aggregation of 1-dodecyl-3-methylimidazolium nitrate in water and benzene studied by SANS and ^{1}H NMR, Phys. Chem. Chem. Phys. 14 (2012) 11070–11080.
[35] L. Suo, O. Borodin, T. Gao, M. Olguin, J. Ho, X. Fan, C. Luo, C. Wang, K. Xu, "Water-in-salt" electrolyte enables high-voltage aqueous lithium-ion chemistries, Sci. 350 (2015) 938–943.
[36] M. Becker, D. Rentsch, D. Reber, A. Aribia, C. Battaglia, R.-S. Kühnel, The hydrotropic effect of ionic liquids in water-in-salt electrolytes, Angew. Chem. Int.

Ed. 60 (2021) 14100–14108.

[37] Y. Ishii, N. Matubayasi, G. Watanabe, T. Kato, H. Washizu, Molecular insights on confined water in the nanochannels of self-assembled ionic liquid crystal, Sci. Adv. 7 (2021) eabf0669–14.

[38] D. Műnoz-Santiburcio, D. Marx, Chemistry in nanoconfined water, Chem. Sci. 8 (2017) 3444–3452.

[39] H.R. Corti1, G.A. Appignanesi, M.C. Barbosa, J. Rafael Bordin, C. Calero, G. Camisasca, M. Dolores Elola1, G. Franzese, P. Gallo, A. Hassanali, K. Huang, D. Laria, C.A. Meńendez, J.M. Montes de Oca, M. Paula Longinotti, J. Rodriguez, M. Rovere, D. Scherlis, I. Szleifer, Structure and dynamics of nanoconfined water and aqueous solutions, Eur. Phys. J. E 44 (2021) 136–150.

[40] H. Abe, H. Kishimura, Multistep phase transition in 1-decyl-3-methylimidazolium nitrate ionic Liquid, J. Mol. Liq. 352 (2022) 118695–1118650.

[41] T. Arii, A. Kishi, Y. Kobayashi, A new simultaneous apparatus for X-ray diffractometry and differential scanning calorimetry (XRD-DSC), Thermochim. Acta 325 (1999) 151–156.

[42] N.V. Sastry, N.M. Vaghela, P.M. Macwan, Densities, excess molar and partial molar volumes for water + 1-butyl- or, 1-hexyl- or, 1-octyl-3-methylimidazolium halide room temperature ionic liquids at T = (298.15 and 308.15) K, J. Mol. Liq. 180 (2013) 12–18.

[43] H. Abe, F. Nemoto, K. Hiroi, K. Ohishi, S. Takata, Spontaneous formations of nanoconfined water in ionic liquids by small angle neutron scattering, J. Mol. Liq.

346 (2022) 117035–117036.

[44] S. Takata, J. Suzuki, T. Shinohara, T. Oku, T. Tominaga1, K. Ohishi, H. Iwase, T. Nakatani, Y. Inamura, T. Ito, K. Suzuya, K. Aizawa, M. Arai, T. Otomo, M. Sugiyama, The Design and q Resolution of the Small and Wide Angle Neutron Scattering Instrument (TAIKAN) in J-PARC, JPS Conf. Proc. 8 (2015) 036020–036026.

[45] H. Abe, M. Aono, T. Takekiyo, Y. Yoshimura, A. Shimizu, Phase behavior of water-mediated protic ionic liquid: Ethylammonium nitrate, J. Mol. Liq. 241 (2017) 301–307.

[46] E. Paineau, M.-E.-M. Krapf, M.-S. Amara1, N.V. Matskova, I. Dozov, S. Rouzie're, A. Thill, P. Launois, P. Davidson, A liquid-crystalline hexagonal columnar phase in highly-dilute suspensions of imogolite nanotubes, Nature Commun. 7 (2016) 10271–10278.

[47] W. Cao, Y. Wang, G. Saielli, Metastable State during Melting and Solid−Solid Phase Transition of $[C_n Mim][NO_3]$ (n = 4–12) Ionic Liquids by Molecular Dynamics Simulation, J. Phys. Chem. B 122 (2018) 229–239.

[48] M. Xu, J.P. Larentzos, M. Roshdy, L.J. Criscenti, H.C. Allen, Aqueous divalent metal–nitrate interactions: hydration versus ion pairing, Phys. Chem. Chem. Phys. 10 (2008) 4793–4801.